

Simulation of transverse wood compression using a large-deformation, hyperelastic–plastic material model

Yamina E. Aimene · John A. Nairn

Received: 23 January 2014 / Published online: 10 October 2014
© Springer-Verlag Berlin Heidelberg 2014

Abstract Transverse compression of wood is a process that induces large deformations. The process is dominated by elastic and plastic cell wall buckling. This work reports a numerical study of the transverse compression and densification of wood using a large-deformation, elastic–plastic constitutive law. The model is isotropic, formulated within the framework of hyperelasticity, and implemented in explicit material point method (MPM) software. The model was first validated for modeling of cellular materials by compression of an isotropic cellular model specimen. Next, it was used to model compression of wood by first validating use of isotropic, transverse plane properties for tangential compression of hardwood, and then by investigating both tangential and radial compression of softwood. Importantly, the discretization of wood specimens used MPM methods to reproduce accurately the complex morphology of wood anatomy for different species. The simulations have reproduced observations of stress–strain response during wood compression including details of inhomogeneous deformation caused by variations in wood anatomy.

Introduction

Compression is an important deformation mechanism in many wood-manufacturing processes, such as for processing of wood-based composites and structural components. At large deformations, transverse wood compression involves

Y. E. Aimene (✉)

University of French West Indies and Guiana – Ecofog, 97306 Cayenne, France
e-mail: yamina.aimene@guyane.univ-ag.fr

J. A. Nairn

Wood Science and Engineering Department, Oregon State University, Corvallis, OR 97330, USA

nonlinear elastic–plastic behavior (Bodig 1963, 1965, 1966; Dinh 2011). The elastic–plastic behavior is confirmed by observations at the microscopic scale and is related to anatomical features of wood specimens, such as wood density, percentage of latewood and earlywood, ray volume, etc. and to loading direction. Figure 1 shows a typical stress–strain curve for transverse wood compression. The curve begins with a quasi-linear elastic region at small strain. It is followed by a quasi-plateau region and then by a zone of increasing stress at high strain—the densification region. The plateau region corresponds to cell collapse at a quasi-constant stress. It results from elastic and plastic buckling instabilities in the cell wall microstructure or to fracture of those cell walls (Holmberg 1998). The densification region corresponds to cell walls contacting each other, after complete collapse. For wood with highly heterogeneous rings, such as softwoods, tangential compression gives rise to buckling of latewood regions that are not supported by earlywood regions, whereas radial compression produces buckling in the earlywood cells first (Persson 2000).

Wood compression is dominated by the role of its morphology, e.g., the cellular structure of wood. Several models have attempted to model this behavior. Gibson et al. (1982) developed 2D and 3D analytical models for deformation and buckling of a regular array of hexagonal cells. The assumptions inherent in these models limit them to very low-density structures that are not sufficiently accurate for typical wood densities. A few finite element models have looked at deformation of cellular structures. These models are typically limited to idealized morphologies (Zhu et al. 1997; Rangri 2004) or to only a small number of wood cells [e.g., a single cell by Shiari and Wild (2004)]. Lattice models were suggested as a potential morphology-based tool in which cell walls are represented by rods and springs with appropriate properties (Landis et al. 2002; Davids et al. 2003; Smith et al. 2003). These models are not able to handle both the complex morphology of wood and its real mechanical behavior. Recently, a finite element model for describing the nonlinearities of wood under compression was developed (Oudjene and Khelifa 2009a, b). They modeled

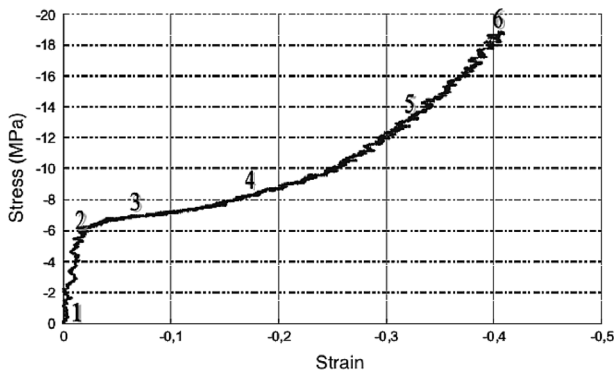


Fig. 1 Experimental stress–strain curve for tangential poplar wood compression (Dinh 2011). The numbers correspond to phases in compressive strain: 1–2 is the elastic phase; 2–4 is the plateau region; 4–6 contains the onset of densification

wood as a 3D orthotropic continuum including an anisotropic hardening law and ductile densification. A continuum method, however, does not model the cellular structure and therefore does not give insights into the role of cell wall contact or heterogeneous anatomy on wood compression.

In contrast to the commonly modeled regular cellular arrays, the compression of wood is affected by wood anatomy that includes variations in cell size (earlywood vs. latewood), types of wood cells (softwood anatomy vs. hardwood anatomy), and different organization of cells in radial and tangential directions. The development of improved numerical simulations of wood transverse compression requires a numerical tool that can include a realistic description of wood anatomy and therefore account for variations in cells within a single specimen and between different specimens. The extension into the densification region requires a numerical tool that can handle massive amounts of contact along with large deformation and rotation. The material point method (MPM) appears to be a powerful numerical tool that can handle complex wood anatomy, cell wall contact, and large deformations and rotations.

This paper describes MPM simulations of transverse compression and densification of wood. An isotropic, hyperelastic–plastic model was used to model transverse cell wall properties. The approach was first validated by simulating compression of a cellular structure with a small number of cells, which could be directly compared to experiments of a model made with an isotropic material. Within the assumption of the homogeneity of transverse cell wall properties, the model was then used to identify the average wood properties for simulation of tangential compression of hardwood. The features of the modeling were validated by comparison to experimental data and showed the simulation reproduces key features of the stress–strain curve and many features of the local deformation processes. The model was then used to study both radial and tangential transverse wood compression and densification of a softwood species. Similar MPM modeling was previously used to model wood compression (Nairn 2006). The goal here was to extend that work to more realistic, large-deformation, elastic–plastic material models and to more profound validation. The new validation was done by direct comparison of simulation results to compression experiments on a model cellular structure and on wood.

Methods

MPM was developed as an alternative tool for numerical modeling of dynamic solid problems (Sulsky et al. 1994; Zhou 1998; Bardenhagen et al. 2001; Bardenhagen and Kober 2004; Nairn 2003, 2007, 2013; Sadeghirad et al. 2011). In MPM, a solid body is discretized into points, called particles, much as a computer image is represented by pixels. At each time step, the particle information is extrapolated to a background grid. The grid velocities are used to calculate velocity gradients that are input to material models; the constitutive law of the material updates particle stresses and strains and internal forces on the grid. Next, the momentum equation is solved on the grid, and updated grid results are used to update the particle velocities

and positions. This combination of Lagrangian (particle basis) and Eulerian (grid basis) methods has proven useful for solving solid mechanics problems including those with large strains or rotations and involving materials with history-dependent properties such as plasticity or viscoelasticity effects. In addition, MPM can handle contact without needing specially designated elements (Bardenhagen et al. 2001; Nairn 2013). The reader is referred to prior paper on generalized MPM derivation in Bardenhagen and Kober (2004) for more details on specifics of MPM.

MPM is particularly suited to wood compression because of its ease in modeling a realistic wood anatomy. In MPM, there is no need to create a mesh. Rather the complete numerical discretization can be derived directly from SEM images of wood structures simply by translating pixels in the image into material points in the model. Based on the gray value for any location in a bitmapped image, that location is either assigned as cell wall material point or as a vacant space representing cell lumen or other open space in the wood anatomy. This approach was previously used to model wood compression (Nairn 2006); it is extended here to large-deformation material models and to make direct comparisons to experimental observations.

The large-deformation material used here for wood behavior was modeled within a hyperelastic–plastic model formulated in the spatial configuration. It is based on the notion of a stress-free intermediate configuration and uses a multiplicative decomposition of the deformation gradient \mathbf{F} considered by many authors (Sidoroff 1974; Simo 1988a, b; Simo and Hughes 1997) and given by $\mathbf{F} = \mathbf{F}^e \cdot \mathbf{F}^p$, where \mathbf{F}^e and \mathbf{F}^p are, respectively, the elastic and plastic deformation gradient tensors. The elastic response was modeled as a Neo-Hookean material where the elastic strain energy is given by:

$$w = \frac{1}{2} \kappa \left(\frac{1}{2} (J^{e2} - 1) - \ln J^e \right) + \frac{1}{2} \mu (tr(\overline{\mathbf{B}}^e) - 3) \quad (1)$$

Here, $J^e = \det(\mathbf{F}^e)$, $\overline{\mathbf{B}}^e = \overline{\mathbf{F}}^e \cdot \overline{\mathbf{F}}^{eT}$ is the deviatoric part of the left Cauchy–Green strain tensor and $\overline{\mathbf{F}}^e = (J^e)^{-1/3} \mathbf{F}^e$ is the deviatoric part of the elastic deformation gradient. The κ and μ material properties are equal to the low-strain bulk and shear moduli; as such, they are related to low-strain modulus E and Poisson’s ratio ν , by:

$$\kappa = \frac{E}{3(1-2\nu)} \quad \text{and} \quad \mu = \frac{E}{2(1+\nu)}. \quad (2)$$

The elastic stresses are found by differentiation of the elastic strain energy. The plastic response was modeled by yielding at σ_Y following by perfectly plastic response (or no work hardening) using return mapping methods (Simo and Hughes 1997). This material model is isotropic and was implemented in explicit MPM software (NairnMPM) by using a user subroutine. The input from standard MPM code to this subroutine is the incremental deformation gradient, which is sufficient to evaluate and update particle stresses and deformation using the above relations.

For comparison to prior work on wood compression (Nairn 2006) and to other common numerical models of wood, selected simulations were run with a small-strain material model instead of the above large-strain model. The small-strain

model used isotropic Hooke's law for elastic stress and strain and J_2 plasticity theory (Simo and Hughes 1997) to model elastic–plastic behavior, which was the same perfectly plastic response used in the large-deformation material.

The hyperelastic material model was verified by extensive comparison to stress–strain tests on homogeneous specimens. One goal of this work was to check whether the model is useful for modeling cellular materials. Both isotropic cellular materials and anisotropic cell wood material were modeled. Simulations on wood were conducted in the transverse direction. Although wood cell walls, in this direction, have multiple layers of reinforced composite and isotropic materials (Guitard 1987; Astley et al. 1998; Qing and Mishnaevsky 2009), cell wall properties in the transverse plane were assumed isotropic. This assumption is arguable for transverse behavior. Nevertheless, homogeneous elastic properties of cell walls were estimated for many wood species by average values using homogenization method of composite materials, and so, this assumption is very common in wood models, especially those attempting to capture the effect of the geometry of the wood cells on wood stiffness (Koponen et al. 1989; Astley et al. 1998; Harrington et al. 1998). In principle, the cell wall layers could be explicitly modeled, but that approach presents two grand changes—there are not reliable properties for the individual layers, and the resolution required to simultaneously resolve cell wall layers and model a large number of cells would make the simulations too large. In summary, the isotropic assumption is acceptable and the proposed model will help capture the effect of the long-range morphology cell walls. Note that although the cell wall material was modeled as isotropic, the bulk response of a realistic wood cellular structure will be anisotropic due to anatomy of the specimen. For example, the in-plane shear modulus of a cellular structure will be much lower than the shear modulus of the isotropic cell walls. These simulations in the transverse direction and on realistic anatomies can capture such structural anisotropies. The extension of this work to 3D simulations would require hyperelastic, anisotropic material models.

These simulations, especially at high densification, involved massive amounts of contact. Two types of MPM contact features were used. First, as a cellular material is compressed, the cell walls will collapse causing contact with the opposite sides. This self-contact is automatically modeled by MPM because particles are not allowed to penetrate other particles. The ability of MPM to handle self-contact without needing any special methods is an advantage over finite element analysis that typically needs special contact methods such as a priori designation of master and slave elements to be in contact. Assigning master and slave contact surfaces would not be possible here because it is not known in advance where the cell walls will make contact. A limitation of automatic MPM contact is that the contact mechanics is limited to stick conditions. Because uniaxial compression of wood is not likely to promote significant sliding deformation between cell walls, the stick physics should be an acceptable approximation.

The second type of contact modeled was between a rigid piston and the specimen (in some simulations) as the piston pushes on the specimen. This contact loading was handled by multimaterial MPM methods (Bardenhagen et al. 2001). In brief, when extrapolating to the background grid, each material extrapolates to its own velocity field. In subsequent MPM calculations, nodes that are populated by more

than one material combine the results using various methods for contact physics. Multimaterial MPM can model contact by stick, friction (Bardenhagen et al. 2001), or model the contact as an imperfect interface (Nairn 2013). For MPM contact calculations to be accurate, it is important that the simulation accurately finds the normal vector between the contact surfaces (Nairn 2013). In these simulations, the normal vector was constant (normal to the rigid surface). Because the normal vector could be prescribed, the frictional contact during loading should be modeled accurately.

Results and discussion

Validation of material modeling

Figure 2a shows an anatomical cross section of softwood composed of eight selected cells. Figure 2b shows a prototype of that cross section made of polyoxymethylene (POM) to mimic the selected softwood cells (Rangsri 2004). The macroscopic prototype specimen (47.6 mm high and 5 mm thick) was then compressed, while recording force versus deformation and recording images of sequential deformations showing the cell wall buckling process. Because the model is made from a well-characterized isotropic material, it was ideal for us to validate the isotropic, hyperelastic, elastic–plastic material model implemented in MPM for use in cellular materials. This specific geometry and material were modeled, and MPM deformations were directly compared to observed deformations.

The MPM discretization of the POM model was derived from a 428×532 pixel digital image of the model with each cell wall pixel leading to a cell wall material point. The MPM model, shown in Fig. 2c, had 92,875 material points. The top of the specimen was compressed at a constant rate of 10 m/s using a rigid material with load transferred by multimaterial MPM frictional contact methods (Bardenhagen et al. 2001; Nairn 2013) with a coefficient of friction of 0.35. The bottom edge was set to zero vertical velocity, while the bottom left point was restrained to

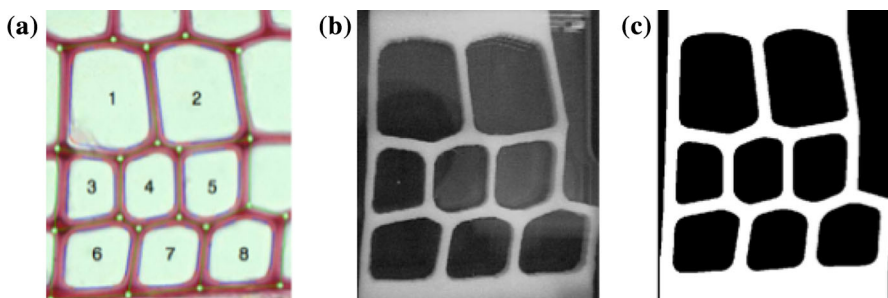


Fig. 2 Cellular material geometry; **a** image of a cross section of softwood anatomy, **b** experimental model specimen made using polyoxymethylene (POM), **c** MPM discretization of the model in B derived from an image of the model specimen

zero horizontal velocity to prevent unstable sliding. The simulations, like all simulations in this paper, used 2D plane strain conditions. The POM cell walls were assumed to have isotropic, hyperelastic–plastic behavior. The elastic properties for POM were $E = 3.1$ GPa, $\nu = 0.4$, and density $\rho = 1.2$ g/cm³, which correspond to $\kappa = 5.166$ GPa and $\mu = 1.071$ GPa. The plastic deformation used yield stress $\sigma_y = 72$ MPa. These properties gave bulk wave speed of 2,344 m/s, which means loading rate of 10 m/s was 0.43 % of the wave speed and could be considered to be quasi-static loading. Note that these quasi-static conditions have eliminated dynamic loading effects, which appear in stress–strain curves at low-frequency vibrations that depend on specimen dimensions. The high-frequency vibrations that remain are numerical oscillations associated with grid-based velocity boundary conditions and contact mechanics, but are not associated with dynamic loading conditions. Also note that density is required because the MPM method solves the dynamic momentum equation, but the results are independent of density in the quasi-static limit.

Figure 3a shows the experimental deformed shapes at various levels of vertical displacement (5.3, 13.6, 27.3, and 42 %, respectively). The corresponded MPM simulations are in Fig. 3b, and all are similar to the experimental shapes. All details observed at different stages of compression were well reproduced at different stages of compressive strain. A key requirement to matching all stages was accounting for plastic deformation. Simulations without plastic yielding did not agree as well, especially in the intermediate states. Figure 3c shows the cumulative plastic strain in MPM calculations. The plastic zones are located at the junctions of the cell walls. In addition, the global and local geometry of the cellular material influenced the formation of the plastic zones. During loading, plastic zones appeared first at the junctions of cells 3, 4, and 5, starting at the left wall of cell 3 (Fig. 3b at 5.3 % of strain). This observation can explain the shape observed during the compression process, which is characterized by the first collapse region observed in cell 3. Then, new plastic zones were developed in cells 1 and 2. This plastic yielding creates a plastic hinge that transforms the initial hyperstatic structure to a mechanism promoting collapse of the cellular structure.

Hardwood compression: tangential direction

The previous section validated MPM methods with a hyperelastic–plastic model for compression of a cellular structure that deforms by plastic buckling of the cell walls. Next, the modeling methods were applied to buckling of a hardwood during transverse compression. The cell wall was assumed to be isotropic (in the transverse plane), but transverse cell wall properties are not known and cannot be measured. The first MPM simulations, therefore, were used to identify transverse cell wall properties by an inverse method. In other words, the cell properties were varied and the best properties were picked by comparing simulation results to experimental data on tangential compression of hardwood (Dinh 2011).

Dinh (2011) presents experimental results on poplar (*Populus*) carried out in an SEM. Figure 4a shows a small part of a larger specimen in a 472×406 pixel image that covered an area of 3.37×2.89 mm². The experimental stress–strain curve is

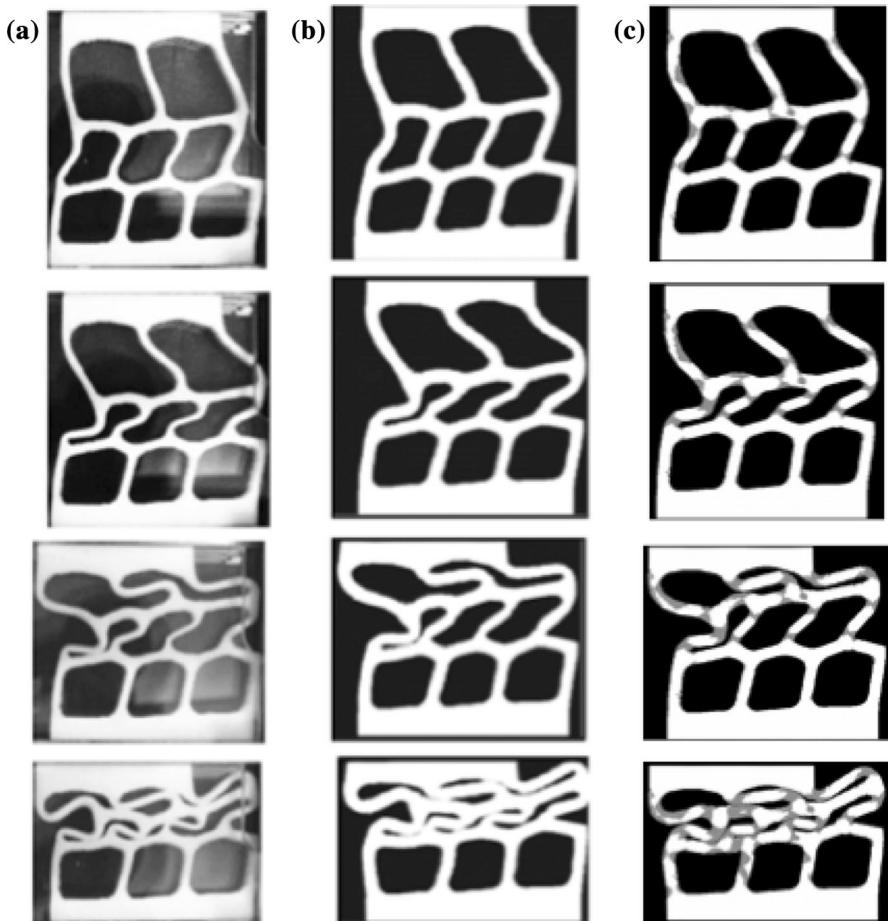


Fig. 3 Deformed shapes at 5.3, 13.6, 27.3, and 42 % relative displacement for the top rigid body; **a** specimen in experimental tests, **b** MPM simulated shapes, **c** cumulative plastic energy in the cell walls from the MPM simulations (zero plastic energy is *white*, and dissipated plastic energy is *gray*)

shown in Fig. 1 (Dinh 2011). This same specimen was modeled using MPM. The MPM model was derived from the SEM image shown in Fig. 4b; this model contained 73,105 material points. The cell wall was assumed isotropic hyperelastic–plastic in the transverse plane, with effective transverse properties representing average values of cell wall properties. These effective properties were estimated by a series of numerical tests, as illustrated in Fig. 5 that fit best the experimental curve given in Fig. 1. The most important cell wall properties were the elastic modulus and the yield stress. Because other properties had less influence on the results, they were selected on the basis of average values expected for cell walls, namely Poisson’s ratio $\nu = 0.33$ and density $\rho_w = 1.5 \text{ g/cm}^3$ (Easterling et al. 1982). All boundary conditions along the edges assumed uniform displacement. The bottom edge of the specimen was restricted to zero vertical velocity; the compression was

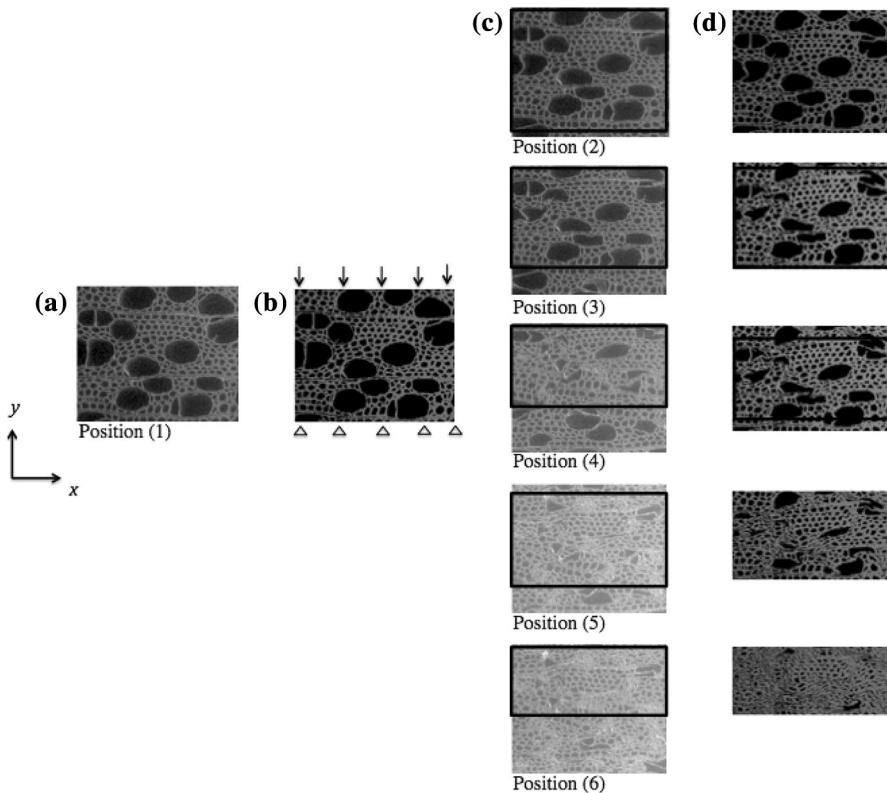


Fig. 4 Snapshots of experiments (from Dinh 2011) and MPM simulations for transverse compression of poplar; **a** SEM micrograph of uncompressed poplar, **b** MPM discretization of the specimen from SEM image with the addition of boundary conditions for tangential compression, **c** experimental shapes at the experimental compressive strains indicated in Fig. 1, **d** MPM simulations at the same displacements with $E_w = 9$ GPa, $\sigma_Y = 120$ MPa, and $\nu_{TR} = 0.25$. Because the experiments shifted in the SEM images, the *squares* in column (c), the portions that correspond to the simulated region, whereas those in column (d) are the parts of the MPM simulations that match the experiments parts, as under the SEM, the experimental specimen shifted to the bottom

achieved by a rigid piston loading at a constant rate of 10 m/s on the top of the specimen, which is $<1\%$ of the wave speed for the entire range of moduli considered below. The sides were displaced horizontally to represent Poisson's expansion due to compression. The selection of the lateral expansion rate is discussed below. Note that frictional contact on the loading surface was not needed here because the sidewalls prevent sliding of those surfaces.

Figure 5 shows simulated compressive stress–bulk strain curves for various combinations of cell wall modulus and yield strength that best approach the experimental results illustrated in Fig. 1 from Dinh (2011). The initial elastic slope, which experimentally was around 400 MPa (Dinh 2011), could be matched reasonably well with an elastic modulus, E_w , in the range of 5–9 GPa. If the assumed elastic modulus was too low (<4 GPa), the initial slope was lower than experimental results. The plateau stress was influenced most by the yield stress, but

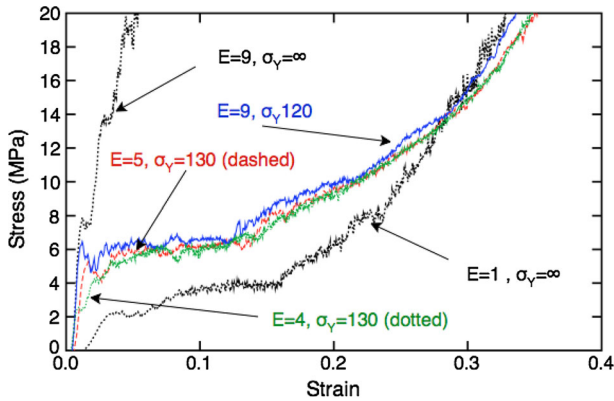


Fig. 5 Simulated compressive stress–bulk strain curves for various combinations of cell wall modulus (in GPa) and yield strength (in MPa)

the appropriate yield stress depended on the elastic modulus. With $E_w = 5$ GPa, the plateau was matched well with a yield stress of $\sigma_Y = 130$ MPa. With $E_w = 9$ GPa, the plateau was matched best with a yield stress of $\sigma_Y = 120$ MPa. A large extent of the plateau fit well with these property pairs, which implies that an elastic–plastic material with no hardening is a reasonable model for this material. When significant plastic hardening was added to the modeling, the plateau increased faster than experimental results.

The best numerical strain–stress curves reproduced the global behavior of the experimental results (see “ $E = 9, \sigma_Y = 120$ ” and “ $E = 5, \sigma_Y = 130$ ” curves in Fig. 5 vs. Fig. 1). The curves clearly show the characteristic regions of transverse wood compression: an elastic region, a plastic plateau, and then a densification region of increasing stress. The densification region occurs when cell walls begin self-contact, which is automatically handled by the MPM model. The experimental and numerical results do show some differences, especially around the densification region. The assumption in the MPM simulations of homogeneity of the wooden cell walls and its mechanical properties could have contributed to these differences, as well as a 3D effect that is not taken into account in plane strain calculations.

Another difficulty is that the MPM simulations were restricted to a portion of the specimen rather than the entire specimen used in experiments. Because of this issue, it was difficult to select appropriate boundary conditions by reproducing the actual displacements on the edges of the modeled volume. One modification was used to account for edge effects. The top and bottom surfaces assumed affine deformation, which corresponds to constant displacement rate on the top and zero displacement rate on the bottom. To mimic Poisson’s expansion in the horizontal direction, the lateral sides were displaced at a constant rate given by:

$$v_x = -v_{\text{TR}} \frac{v_y w}{2h} \quad (3)$$

where v_{TR} is T-R Poisson’s ratio of bulk wood, v_y is the vertical displacement rate, and w and h are the width and height of the modeled volume. The value for v_{TR} was

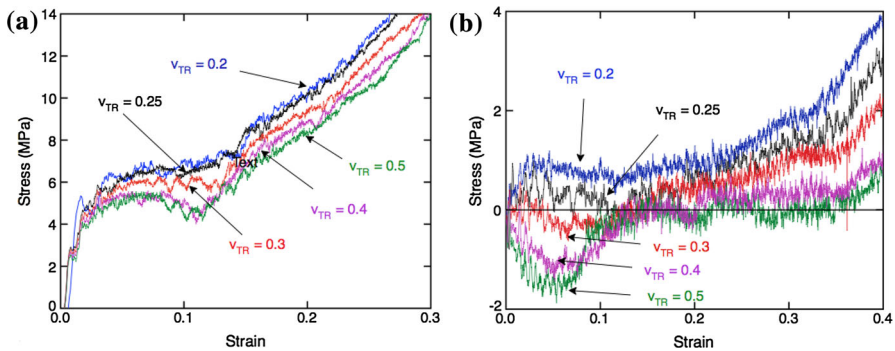


Fig. 6 **a** Compressive stress–bulk strain curves for different lateral strains as determined by assumed value for bulk v_{TR} , **b** the corresponding reaction stresses induced on the sidewalls (note that the stress axis is greater expanded for these small reaction stresses)

adjusted such that the reaction forces on the lateral wall boundary conditions were as close to zero as possible. Figure 6a shows the stress–strain curves for different values of v_{TR} from 0.2 to 0.5. Figure 6b shows the corresponding lateral reaction pressure where a positive pressure is the wall compressing the wood (note that the y-axis is greatly expanded in Fig. 6b vs. 6a to better visualize the smaller lateral forces). The lateral reaction pressure decreased as v_{TR} increased, but for $v_{TR} > 0.3$, the lateral rate became negative at low strain. These $v_{TR} > 0.3$ results were deemed to have too much lateral motion because the negative pressure induced splitting of cell walls at low strain (i.e., tensile stress on the wood). No value for v_{TR} maintained zero lateral stress for all strains. $v_{TR} = 0.25$ was used as the best approximation. It maintained low level of reaction force except in the densification region. The rise of lateral stress in the densification regime may be another reason why the simulations and experiments deviated at the highest strains.

Finally, Fig. 4c, d compares snapshots of the simulated deformed geometry using optimized properties and boundary conditions to SEM images from experimental results at various compressive strains (Dinh 2011). Many deformation features are reproduced well by MPM simulations, especially at the beginning where globally the MPM boundary conditions are most accurate. The experimental specimen undergoes less compressive strains in the tangential direction than the numerical specimen. This difference could be caused by the simulation only considering a portion of the sample rather than the entire specimen. For example, the random morphology of wood could generate heterogeneous compression such that the analyzed section might be seeing a different level of compression than other regions of the specimen, while the numerical model assumed that the compression on the modeled specimen matched the globally applied compression.

In summary, MPM simulations that accurately represent the complex wood anatomy and assume homogeneity of transverse cell wall properties using an isotropic hyperelastic–plastic material, correctly represent the key observations in tangential compression of poplar, including the elastic zone, the plateau region, and the densification zone. The hardest zone to model is the densification zone at large

strains. In addition to use a 2D plane strain model and the challenges of selecting boundary conditions, it is possible that the assumption of isotropy in the transverse plane becomes less accurate at high strains.

Softwood compression

The previous two sections validated MPM models for compression of cellular structures including hardwood compression with a complex anatomy. Next, the model was used to better understand the behavior of softwood during both tangential and radial compression. To achieve this goal, transverse compression of mature loblolly pine (*Pinus taeda*) was modeled based on an SEM image of a transverse section of wood taken at the intersection of two growth rings, composed of earlywood and latewood. The SEM micrograph image's resolution was 360×234 pixels, and its area was $0.832 \times 0.541 \text{ mm}^2$ (Fig. 7a, from Kultikova 1999). Although no experimental results for comparison were available, this same image was modeled by MPM before using a small-strain elastic–plastic material (Nairn 2006).

The cell wall material was assumed isotropic in the transverse plane with an elastic modulus $E_w = 10.6 \text{ GPa}$, a Poisson's ratio $\nu = 0.33$, and a density $\rho_w = 1.5 \text{ g/cm}^3$. The plastic properties were estimated by a yield stress $\sigma_Y = 500 \text{ MPa}$ with no hardening. These are average values resulting from interpretation of experiments reported by Tabarsa (1999) and Tabarsa and Chui (2000, 2001).

The boundary conditions for radial compression are illustrated in Fig. 7b. The left side of the specimen was restrained to zero velocity (hashed edge), and the right side was compressed with a rigid body at a constant rate. The top and bottom were restrained to zero vertical velocity (solid black lines). For simulations of tangential compression, the boundary conditions in Fig. 7b were rotated 90° ; in other words, the topside was compressed with a rigid body, while the bottom, left, and right sides were constrained to zero velocity. All simulations used 2D, quasi-static plane strain conditions. The compression rate in both directions was 10 m/s , which is $<0.4 \%$ of the longitudinal wave speed of the cell wall material ($2,650 \text{ m/s}$).

Softwood: radial compression

For comparisons, the simulations in this section used both the large-strain hyperelastic model validated in this work for cellular compression and the small-strain model that was used in prior work on wood compression (Nairn 2006). Both models were elastic, perfectly plastic. Figure 8 shows the applied stress as a function of compression up to compressive strain of 0.75 for both material models using identical cell wall mechanical properties. Figure 8a shows the full curve, while Fig. 8b is an enlargement of the low-strain regime better showing the plastic plateau. Both models show all compressive regimes including initial elastic slope, quasi-plateau, and densification regimes.

The hyperelastic–plastic model should more realistically model wood transverse compression, especially at large strain. The results show the large-deformation model requires less applied stress than the low-strain model to compress the

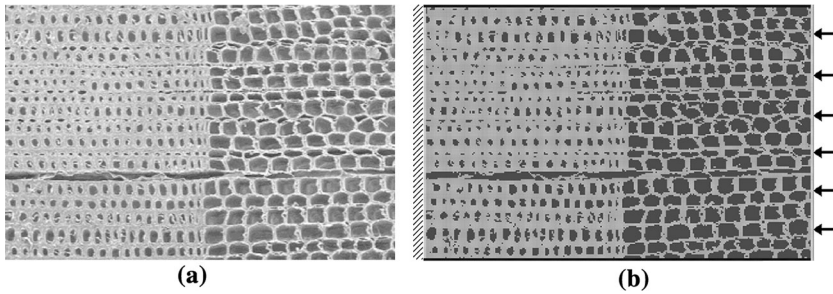


Fig. 7 **a** SEM micrograph of uncompressed mature loblolly pine (from Kultikova 1999), **b** MPM discretization with boundary conditions for radial compression where *left, top, and bottom* are constrained to zero velocity and the right side is compressed at constant velocity

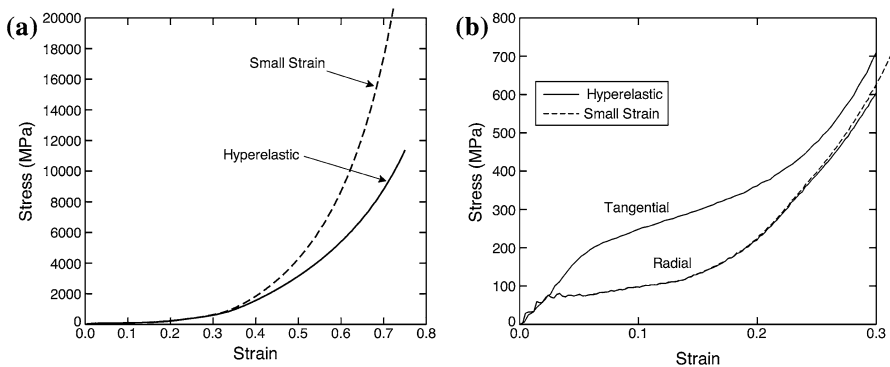


Fig. 8 Applied stress as a function of bulk compressive strain during simulated radial compression in loblolly pine using a small-strain elastic–plastic and a hyperelastic–plastic model; **a** the full curve, **b** enlargement of the low-strain regions with the addition of tangential compression using a hyperelastic–plastic model

specimen. These results are paradoxical because the hallmark of large-deformation models is that they stiffen under compression and therefore require higher load to get to same compressive strain as a low-strain model. This paradox is explained by looking at particle results and by realizing the model is of a cellular structure and not a homogenous bulk material. Figure 9a plots the average particle strain as a function of compressive strain. In a realistic model, the average particle strains should always be less than the bulk strain (the difference being due to remaining void space) and should approach the global strain in the densification regime. Indeed, the large-deformation model meets these expectations. In contrast, the average particle strain in the low-strain model exceeds the global strain and even exceeds 100 %, both of which are physically impossible. The unrealistic, large strain explains when the small-strain model has higher stress as confirmed by looking at particle stresses. When a material has voids, the bulk, or apparent stress, σ_{app} , should be equal to:

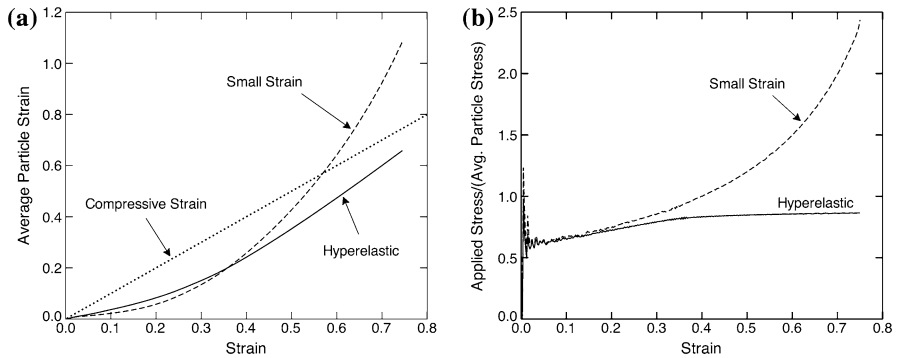


Fig. 9 **a** Average strain in particles for small-strain and hyperelastic models versus bulk strain; the *diagonal line* is the applied bulk strain, **b** applied stress to average particle stress ratio versus bulk strain for small-strain and hyperelastic models

$$\sigma_{\text{app}} = \langle \sigma_p \rangle V_p \quad (4)$$

where $\langle \sigma_p \rangle$ is the average stress on particles and V_p is the volume fraction of space currently filled by particles. The expectation is that at low strain, V_p should be equal to the initial cell wall volume fraction. As compression proceeds, V_p should asymptotically approach one as the material is compressed to a solid continuum, but should never exceed one. The results for $\sigma_{\text{app}}/\langle \sigma_p \rangle$, which should equal V_p , for softwood radial compression, are given in Fig. 9b. At low strain, both models show volume fraction of about 0.60. Although this volume fraction is higher than expected for bulk wood (because it corresponds to bulk density of 0.9 g/cm^3 , which is higher than pine), it corresponds closely to the volume fraction resolved by the SEM image. As mapped to the grid, the SEM image resulted in 50,738 material points over an imaged area with $360 \times 234 = 84,240$ pixels; this modeled image therefore simulated a cell wall volume fraction of 0.60—essentially identical to simulation results. It is higher than bulk pine because the imaged area includes a significant amount of high-density latewood and/or the methods used to prepare the SEM surface caused cells walls to appear thicker than they are interior to the wood. At high compression, the relative stress, $\sigma_{\text{app}}/\langle \sigma_p \rangle$, should approach one as porosity is removed due to densification, but might remain below one if some residual porosity is locked by the structure. This expectation is met by the large-deformation model, but the low-strain model gave poor results and higher stresses.

The unrealistic strains arising in low-strain model calculations can be visualized by plotting all material points that are transformed from their initial square shape into parallelograms by the deformation gradient on each particle. In high-quality MPM results, this visualization method should show particles that completely fill space. Some gaps between particles are inevitable as straight-sided parallelograms cannot completely represent curved deformation fields, but large gaps between particles are indicative of inaccurate simulations or unrealistic material models. Figure 10a, which focuses on a few particles in the middle of the object at high compressive strain, shows that hyperelastic–plastic material points do an excellent

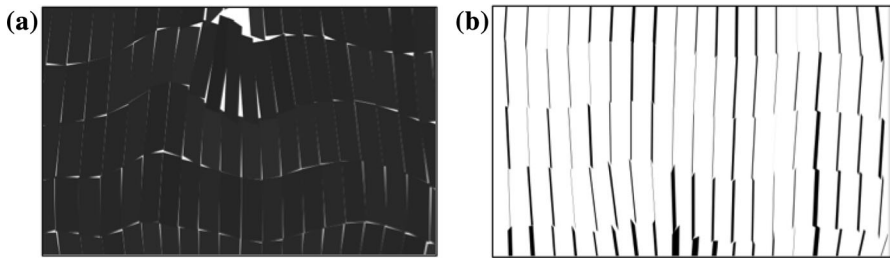


Fig. 10 Enlargement of a material point interior to the object plotted as parallelograms that are deformed from the initial *square* shape by the particle's deformation gradient; **a** using large-strain model, **b** using small-strain model

job of simulating a densified specimen. All space is filled, and only small gaps are seen along the straight sides of the parallelograms. In contrast, Fig. 10b shows that particles using a small-strain model have degenerated into thin lines (caused by compressive strain exceeding 100 %) leaving large, unrealistic gaps in the densified geometry. The hyperelastic–plastic material gives potentially realistic results, while the small-strain model becomes unrealistic at high compressive strain.

Although differences between the two models are significant at high compression ($\varepsilon > 0.3$), which implies a large-deformation material model is essential for modeling high compression, the results given by these two models are closer for low strain (Fig. 8b). Because hyperelastic models converge to small-strain models at low strains, the results should be the same at low strain; Fig. 8b shows they remain similar up to about $\varepsilon = 0.2$, but start to diverge for higher strain. The reason a low-strain model works as high as $\varepsilon = 0.2$ is because bulk applied strain is higher than the particle strain, which is about 0.06 when $\varepsilon = 0.2$ (see Fig. 9a). Finally, the plateau in the low-strain plot shows that plastic deformation begins at very small strain ($\varepsilon = 0.03$). In other words, almost the entire compression process is dominated by plasticity, and simulations require large-deformation plasticity models for valid results over the entire deformation process.

Figure 11 shows snapshots at various compressive strains. At low strain, the plastic is energy confined to the earlywood, starting closer to loaded edge of the specimen. In fact, the thin cell walls of the earlywood lead to an early buckling in this region. This earlywood buckling agrees with experimental observation by many authors (Bodig 1965; Tabarsa and Chui 2000) and with mechanics model expectations. The plastic zone in earlywood continues until nearly all the earlywood has plastically deformed and cell walls are beginning contact, which happens at a compressive strain of about 0.25. At high strain, the plastic zone moves into the latewood. Finally, the densification zone corresponds to generalized plasticity over the entire specimen, when all cell walls are in contact.

Experimental observations for foams suggest that the densification regime begins at a densification density of $\varepsilon_D = 1 - 1.4 \rho/\rho_w$ (Gibson and Ashby 1997). For the simulations here, this result predicts $\varepsilon_D = 0.15$. This prediction does not agree with simulations. Although Fig. 8b does show a kink around compressive strain of 0.15, the snapshots in Fig. 11 clearly show plasticity is still confined to earlywood and

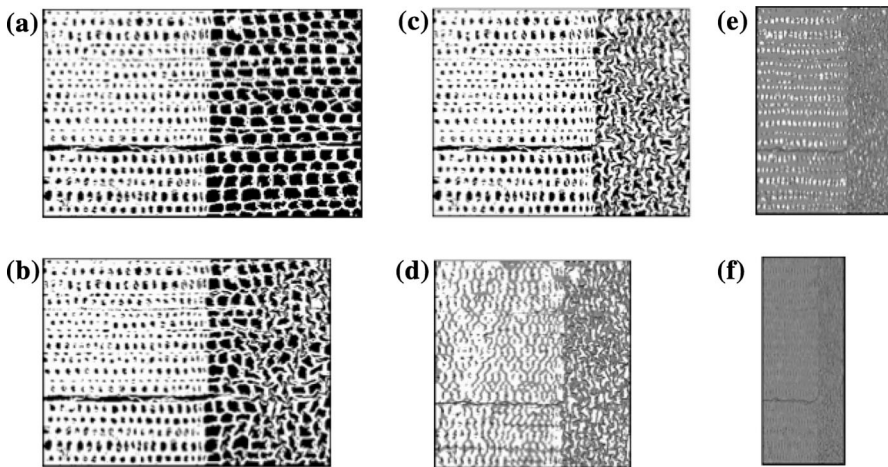


Fig. 11 Plots of cumulative plastic energy in radial wood compression at different stages of compressive strain; **a** 0.02, **b** 0.15, **c** 0.25, **d** 0.4, **e** 0.6, **f** 0.75. Zero plastic energy is *white*, and dissipated plastic energy is *gray*

therefore the latewood is far from the densification regime. The problem with the Gibson and Ashby (1997) result is that it was based on very low-density foams. Although wood is a cellular material, its relative density is much higher than typical foams, which causes some of the approximations used in low-density cellular mechanics to become inaccurate. Another prediction for densification density is to assume it begins when all void space has been removed or when strain equals porosity— $\varepsilon_D = 1 - \rho/\rho_w$. For these simulations, the prediction is $\varepsilon_D = 0.4$. The full stress–strain curve does not have any distinguishing feature around 0.4, but the relative stress plot does show the particle volume reaches a constant plateau above $\varepsilon = 0.4$. The plateau in particle volume when using an accurate large-deformation model is likely a good indicator of the densification regime. The reason the global stress–strain curve does not show the sharp features seen in low-density foams is the relative stiffness between densified and undensified wood is much smaller than between densified and undensified low-density foam. In wood, the transition is gradual rather than sharp as in foams (Gibson and Ashby 1997).

Softwood: tangential compression

Differences in tangential wood compression compared to radial wood compression can be visualized by plotting cumulative plastic energy at various stages of compression. Figure 12 has snapshots of plastic energy during tangential compression to be compared to radial compression results in Fig. 11. At small tangential compression strain, cumulative plastic energy is located mostly in latewood, starting at the opposite side of the moving edge. The initiation of plastic energy is in latewood regions with local density lower than the bulk latewood density, due to

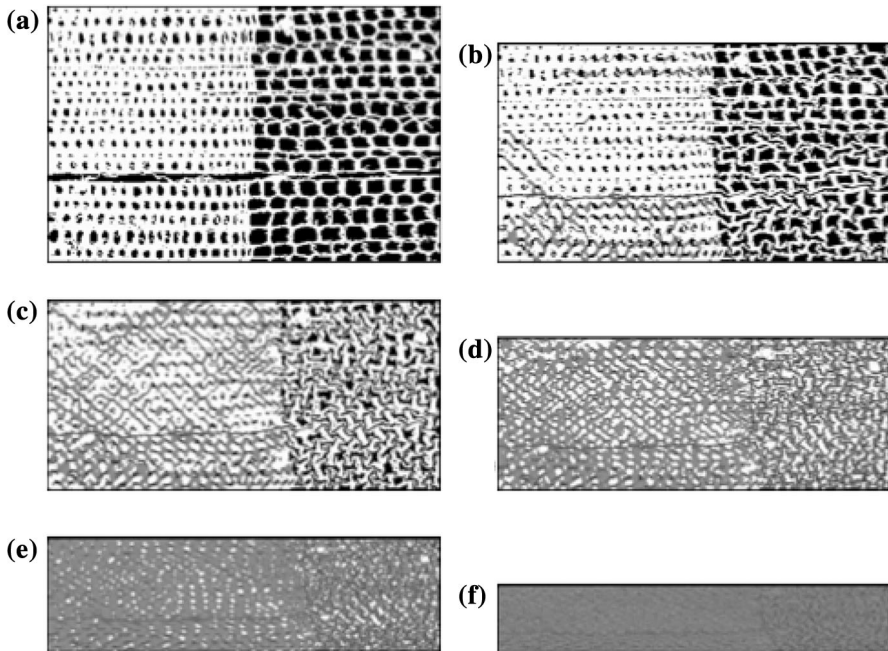


Fig. 12 Plots of cumulative plastic energy in tangential wood compression at different stages of compressive strain; **a** 0.03, **b** 0.15, **c** 0.25, **d** 0.40, **e** 0.60, **f** 0.75. Zero plastic energy is white, and dissipated plastic energy is gray

cell wall stress concentrations in those regions. The plastic zone spreads from the latewood to the earlywood at higher compressive strain.

The deformation processes have a noticeable effect on the stress–strain curves. Figure 8b includes simulated stress–strain curves for both radial and tangential compression. The plateau stress for tangential loading had much higher value than for radial loading. This higher plateau is a consequence of the contribution of latewood plasticity to the yielding process. In contrast, during radial compression, the earlywood can buckle first leading to a much lower plateau. This difference in compression behavior at low strain in softwoods has been observed experimentally by Bodig (1965) and Tabarsa and Chui (2000). As compressive strain increased, the radial and tangential curves converged and became very close in the densification regime. In this regime, all cell walls are in contact and the results are expected to be independent of initial loading process.

The simulated unit cell in Fig. 12 contained only a single growth ring and a single, rather thick, latewood region. Larger specimens with multiple growth rings and/or thinner latewood regions could have different deformation mechanisms, such as buckling of latewood layers that cannot be captured by the unit cell in Fig. 12. Such simulations would be possible by MPM, but would require a very large number of material points to simultaneously capture both long-range effects and cell wall buckling.

Conclusion

Transverse compression of wood involves elastic and plastic behavior and reaches large strains in the densification regime. A hyperelastic–plastic model in NairnMPM, which is MPM software with multiple capabilities, was able to model realistic, complex anatomy of wood as well as to provide new insights into the behavior at large strains. The model was validated by simulated compression of a model cellular material and then validated for wood compression by comparisons of simulations of hardwood tangential compression (poplar) to experimental results. Despite the heterogeneous, laminar structure of reinforced composite materials of the cell walls in the transverse direction, within an assumption of homogeneity of transverse wood properties, an estimation of poplar’s transverse properties needed by the hyperelastic model was found by a series of simulations and comparisons to experimental stress–strain curves. The model was able to reproduce the experimental stress–strain behavior as well as the deformed shapes of the experimental specimen. Finally, the model was used to analyze transverse compression of softwood, loblolly pine. These simulations showed the importance of using a large-deformation model when the goal is to simulate compression into the densification regime. The simulations also gave insights into onset of the densification regime and the role of wood anatomy. For example, MPM simulations led to insights into the distribution of the cumulative plastic energy, which is critical to many industrial problems including wood-manufacturing processes. MPM simulations of both tangential and radial compression of wood exhibited differences observed experimentally by many authors.

Acknowledgments The authors would like to thank Joseph Gril, CNRS Research Director at University of Montpellier II France, for providing some experimental data.

References

- Astley RJ, Stol KA, Harrington JJ (1998) Modeling the elastic properties of softwood—part II: the cellular microstructure. *Holz Roh Werkst* 56:43–50
- Bardenhagen SG, Kober EM (2004) The generalized interpolation material point method. *Comput Model Eng Sci* 5(6):477–495
- Bardenhagen SG, Guilkey JE, Roessig KM, Brackbill JU, Witzel WM, Foster JC (2001) An improved contact algorithm for the material point method and application to stress propagation in granular materials. *Comput Model Eng Sci* 2:509–522
- Bodig J (1963) The peculiarity of compression of conifers in radial direction. *For Prod J* 13(10):438
- Bodig J (1965) The effect of anatomy on the initial stress–strain relationship in transverse compression. *For Prod J* 15:197–202
- Bodig J (1966) Stress–strain relationship for wood in transverse compression. *J Mater* 1:645–666
- Dauids WG, Landis EN, Vasic S (2003) Lattice models for the prediction of load-induced failure and damage in wood. *Wood Fiber Sci* 35:120–134
- Dinh AT (2011) Comportement élastique linéaire et non-linéaire du bois en relation avec sa structure (in French). Dissertation, AgroParisTech, France
- Easterling KER, Harrysson LJ, Gibson LJ, Ashby MF (1982) On the mechanics of balsa and other woods. *Proc R Soc Lond A* 383:31–41
- Gibson LJ, Ashby MF (1997) Cellular solids. Structure and properties. Cambridge University Press, Cambridge
- Gibson LJ, Ashby MF, Schajer GS, Robertso CI (1982) The mechanics of two-dimensional cellular materials. *Proc R Soc Lond A* 382:25–42

- Guitard D (1987) Mechanics of wood and composite materials (Mécanique du matériau bois et composites) (in French) In: Coll Nabla. Cépadues éditions, Toulouse. 228p
- Harrington JJ, Booker R, Astley RJ (1998) Modeling the elastic properties of softwood—part I: the cell-wall lamellae. *Holz Roh Werkst* 56:37–41
- Holmberg SA (1998) A numerical and experimental study of initial defibration of wood. Technical report, Lund University—Lund Institute of Technology—Division of structural Mechanics, Sweden
- Koponen S, Toratti T, Kanerva P (1989) Modeling longitudinal elastic and shrinkage properties of wood. *Wood Sci Technol* 23:55–63
- Kultikova EV (1999) Structure and properties relationships of densified wood. MS Thesis, Virginia Polytechnic Institute and State University
- Landis EN, Vasic S, Davids WG, Parrod P (2002) Coupled experiments and simulations of micro-structural damage in wood. *Exp Mech* 42:389–394
- Nairn JA (2003) Material point method calculations with explicit cracks. *Comput Model Eng Sci* 4:649–664
- Nairn JA (2006) Numerical simulations of transverse compression and densification in wood. *Wood Fiber Sci* 38:576–591
- Nairn JA (2007) Numerical implementation of imperfect interfaces. *Comput Mater Sci* 40:525–536
- Nairn JA (2013) Modeling imperfect interfaces in the material point method using multimaterial methods. *Comput Model Eng Sci* 92:271–299
- Oudjene M, Khelifa M (2009a) Finite element modeling of wooden structures at large deformations and brittle failure prediction. *Constr Build Mater* 30:408–4087
- Oudjene M, Khelifa M (2009b) Elasto–plastic constitutive law for wood behavior under compression loadings. *Constr Build Mater* 23:3359–3366
- Persson K (2000) Micromechanical modeling of wood fiber properties. Dissertation, Department of Mechanics and Materials, Lund University, Sweden
- Qing H, Mishnaevsky L Jr (2009) 3D hierarchical computational model of wood as a cellular material with fibril reinforced, heterogeneous multiple layers. *Mech Mater* 41:1034–1049
- Rangsri W (2004) Experimental and numerical study wood indentation test (Etude expérimentale et numérique de l'essai d'indentation du bois) (in French), Dissertation, Université de Montpellier II, France
- Sadeghirad A, Brannon RM, Burghardt J (2011) A convected particle domain interpolation technique to extend applicability of the material point method for problems involving massive deformations. *Int J Numer Methods Eng* 86(12):1435–1456
- Shiari B, Wild PM (2004) Finite element analysis of individual wood-pulp fibers subjected to transverse compression. *Wood Fiber Sci* 36:135–142
- Sidoroff F (1974) Nonlinear viscoelastic model with an intermediate configuration (Un modèle viscoélastique non linéaire avec configuration intermédiaire) (in French). *J Mech* 13:679–713
- Simo JC (1988a) A framework for finite strain elastoplasticity based on maximum plastic dissipation and the multiplicative decomposition. part I: continuum formulation. *Comput Methods Appl Mech Eng* 66:199–219
- Simo JC (1988b) A framework for finite elastoplasticity based on maximum plastic dissipation and the multiplicative decomposition. part II: computational aspects. *Comput Methods Appl Mech Eng* 68:1–31
- Simo JC, Hughes TJR (1997) *Computational inelasticity*. Springer, New York
- Smith I, Landis E, Gong E (2003) *Fracture and fatigue in wood*. Wiley, New York
- Sulsky D, Chen Z, Schreyer HL (1994) A particle method for history-dependent materials. *Comput Methods Appl Mech Eng* 118:179–196
- Tabarsa T (1999) Compression perpendicular-to-grain behavior of wood. Dissertation, University of New Brunswick, Canada
- Tabarsa T, Chui YH (2000) Stress–strain response of wood under radial compression. Part I. Test method and influences of cellular properties. *Wood Fiber Sci* 32:144–152
- Tabarsa T, Chui YH (2001) Characterizing microscopic behavior of wood under transverse compression, Part II. Effect of species and loading direction. *Wood Fiber Sci* 33:223–232
- Zhou S (1998) The numerical prediction of material failure based on the material point method. Dissertation, University of New Mexico
- Zhu HX, Mills NJ, Knott JF (1997) Analysis of the higher strain compression of open cell foams. *J Mech Phys Solids* 45:1875–1904